

# Vapor annealing synthesis of non-epitaxial $\text{MgB}_2$ films on glassy carbon

A A Baker , L B Bayu Aji , J H Bae, E Stavrou, D J Steich, S K McCall and S O Kucheyev

Lawrence Livermore National Laboratory, Livermore, CA 94550, United States of America

E-mail: [baker97@llnl.gov](mailto:baker97@llnl.gov)

Received 22 December 2017, revised 20 February 2018

Accepted for publication 7 March 2018

Published 29 March 2018



## Abstract

We describe the fabrication and characterization of 25–800 nm thick  $\text{MgB}_2$  films on glassy carbon substrates by Mg vapor annealing of sputter-deposited amorphous B films. Results demonstrate a critical role of both the initial B film thickness and the temperature–time profile on the microstructure, elemental composition, and superconducting properties of the resultant  $\text{MgB}_2$  films. Films with thicknesses of 55 nm and below exhibit a smooth surface, with a roughness of 1.1 nm, while thicker films have surface morphology consisting of elongated nano-crystallites. The suppression of the superconducting transition temperature for thin films scales linearly with the oxygen impurity concentration and also correlates with the amount of lattice disorder probed by Raman scattering. The best results are obtained by a rapid (12 min) anneal at 850 °C with large temperature ramp and cooling rates of  $\sim 540^\circ\text{C min}^{-1}$ . Such fast processing suppresses the deleterious oxygen uptake.

Keywords: superconductivity,  $\text{MgB}_2$ , thin film, levitation

(Some figures may appear in colour only in the online journal)

## 1. Introduction

Magnesium diboride ( $\text{MgB}_2$ ) is one of the most recent additions to the family of technologically relevant superconductors [1]. Interest in  $\text{MgB}_2$  stems from its relatively high superconducting transition temperature ( $T_c$ ) of 39 K, coupled with high critical current densities and critical magnetic fields, comparative ease of fabrication, and a wide range of structures it forms, including wires, thin films, and nanostructures [2, 3]. Some of the proposed applications of  $\text{MgB}_2$  can employ films with submicron thicknesses [2]. These include Josephson-junction bolometers [4], superconductor-based logic devices [5–8], superconducting radio-frequency (RF) cavities [9], and levitation of inertial confinement fusion (ICF) fuel capsules. This latter application, which is the driving force of the present work, requires a smooth thin film of  $\text{MgB}_2$  on the outer surface of a spherical ICF fuel capsule to enable its superconducting levitation in a magnetic field trap.

Levitation of the capsule is conceptually simple, with solenoid coils or permanent magnets positioned outside the hohlraum. The  $\text{MgB}_2$  coating in the superconducting state

acts as a perfect diamagnet and expels the magnetic flux due to the Meissner effect, forcing the field lines to flow around the outer surface of the capsule and producing a Lorentz force that can cancel the gravitational force of the capsule [10]. Although a detailed description of levitation is beyond the purview of this paper, an example is included here to help set context for the ballpark range of the key parameters involved. Our simulations show that an  $\sim 2$  mm diameter capsule weighting  $\sim 7$ –12 mg and coated with an  $\sim 40$ –400 nm thick  $\text{MgB}_2$  outer layer could be levitated 5–6 mm in height above a solenoid coil, providing a magnetic field of 10–30 mT and a current density of 10–1000 A cm $^{-2}$  near the bottom of the capsule, resulting in a Lorentz force of 50–150  $\mu\text{N}$ . Such a levitation-based approach could provide a long-sought-after solution to implosion perturbations caused by conventional fuel capsule support, such as tents or fibers holding the fuel capsule inside a hohlraum [11, 12], which is currently one of the major challenges limiting the ICF implosion yield [13].

Epitaxial superconducting  $\text{MgB}_2$  films with thicknesses down to  $\sim 5$  nm have been demonstrated on single-crystalline substrates including SiC, MgO, and  $\text{Al}_2\text{O}_3$  [2, 14]. Molecular beam epitaxy [15, 16], reactive evaporation [17], and hybrid

physical–chemical vapor deposition (HPCVD) [6, 7, 14] have been particularly successful in making high-quality epitaxial films. In contrast, the growth of non-epitaxial  $\text{MgB}_2$  films on amorphous or polycrystalline substrates has attracted relatively limited attention and yielded less promising results [9, 17–22]. Indeed, non-epitaxial films typically exhibit large surface roughness and reduced  $T_c$  [9, 17–22]. For example, films prepared on glassy carbon substrates by co-deposition of Mg and B followed by annealing at 700 °C had large roughness, depressed  $T_c$  values of 25–30 K, and compositional non-uniformity manifested as the Mg/B ratio varying as a function of depth [19, 20].

Here, non-epitaxial  $\text{MgB}_2$  films were fabricated on glassy carbon substrates by one of the most straightforward and scalable methods, based on the thermal processing of ‘precursor’ B films in Mg vapor [5]. Glassy carbon is chosen to represent the surface of carbon-based ICF fuel capsules, while sputtering is the method of choice for the eventual deposition on non-planar surfaces. We focus on how the elemental composition, microstructure, and superconducting properties of  $\text{MgB}_2$  films are influenced by the precursor B film thickness and (often overlooked) details of the annealing temperature–time profile,  $T(t)$ . Our results reveal a strong influence of the annealing  $T$  ramp rates and dwell times and a clear correlation between O impurity content, lattice disorder, and  $T_c$ .

## 2. Experiment

Films of  $\text{MgB}_2$  were made by exposing precursor B films to Mg vapor at elevated temperatures [5]. This results in the diffusion of Mg into B, accompanied by the  $\text{Mg} + 2\text{B} \rightarrow \text{MgB}_2$  reaction [5, 23–25]. The precursor B films were deposited onto 0.635 mm thick glassy carbon substrates (Marubeni America Corp.) by RF magnetron sputtering of a 50 mm diameter B target (99.9% purity, Plasmaterials, Inc.), with a substrate-to-target distance of  $\sim 57$  mm, a RF power of 200 W, in an Ar atmosphere at a pressure of 12 mTorr in a chamber with a base pressure of  $\sim 5 \times 10^{-7}$  Torr. The deposition rate was  $\sim 5 \text{ nm min}^{-1}$ , and substrate  $T$  during the deposition was limited to  $\sim 55$  °C.

After the deposition,  $\sim 5 \times 5 \text{ mm}^2$  samples were placed in Ta tubes (Eagle Alloys Corp., 99.95% purity; an inner diameter of 10 mm and a length of  $\sim 50$  mm) together with  $\sim 100$  mg of Mg pieces (American Elements, 99.9% purity) and crimped under a  $\text{N}_2$  atmosphere. The sealed Ta tubes were annealed in a 50 mm diameter quartz tube furnace under flowing Ar. We studied the simplest possible shape of the annealing  $T(t)$  profile: a linear ramp to a preset temperature, a single dwell time at this temperature, followed by a cool down to room  $T$ , with the absolute value of the cooling rate matching the ramp rate. Three  $T$  ramp rates of 1, 10, and  $540 \text{ °C min}^{-1}$  were used. The fastest rate was achieved by inserting (removing) a sealed Ta tube into (from) a preheated furnace tube. Boron films with thicknesses of 10, 30, 75, 355, and 450 nm were studied. After Mg vapor annealing, these B

films resulted in  $\text{MgB}_2$  films with thicknesses of 25, 55, 160, 650, and 800 nm, respectively.

The thickness and elemental composition of films before and after Mg vapor annealing were characterized by Rutherford backscattering spectrometry (RBS) with a 2 MeV  $^4\text{He}$  beam. Hydrogen content in selected samples was measured by elastic recoil detection analysis (ERDA) with 3 MeV  $^4\text{He}$  ions. Both RBS and ERDA are nondestructive methods based on high-energy ion scattering, providing depth-resolved information about the elemental composition of near-surface layers [26, 27]. For RBS, the He ion beam was incident normal to the sample surface and backscattered into a detector located at  $165^\circ$  from the incident beam. Hydrogen content was measured with ERDA with the sample normal direction tilted to  $70^\circ$  with respect to the incident beam direction, and hydrogen atoms recoiled at  $150^\circ$  were measured with a surface barrier detector covered with a  $10 \mu\text{m}$  thick carbon foil. The analysis of RBS and ERDA spectra was done with the RUMP code [28].

The surface morphology of films was examined by scanning electron microscopy (SEM) in a JEOL 7401-F microscope operated at 5 kV and by tapping-mode atomic force microscopy under ambient conditions with a Digital Instruments, Inc. Dimension 3000 scanning probe microscope. Single-beam Si cantilever tips with force constants of  $26\text{--}64 \text{ N m}^{-1}$  and resonant frequencies of  $153\text{--}200 \text{ kHz}$  were used. Raman scattering measurements were performed in a backscattering configuration with the 514.5 nm line of an Ar laser. The probing laser spot size was  $\sim 2 \mu\text{m}$ . Spectra in a broad region of  $10\text{--}4000 \text{ cm}^{-1}$  were measured with a spectral resolution of  $2 \text{ cm}^{-1}$  and an acquisition time of 20 s. The laser intensity was kept  $< 2 \text{ mW}$  to minimize sample heating. An experimental setup capable to record Raman spectra at very low wavenumbers ( $< 10 \text{ cm}^{-1}$ ) with solid state notch filters was used [29].

Measurements of the  $T$  dependence of the magnetic moment ( $M(T)$  and, hence, magnetic susceptibility,  $\chi = M/H$ , where  $H$  is the magnetic field applied), were conducted with a Quantum Design MPMSXL SQUID magnetometer in a field of 100 Oe over the  $T$  range of 5–70 K. Samples were mounted with the film surface parallel to the applied magnetic field and zero field cooled to 5 K prior to  $M(T)$  measurements. Measurements of the critical current density ( $J_c$ ) were conducted by applying the Bean critical state model ( $J_c = 30\Delta M/r$ , where  $r$  is the radius corresponding to total sample size [30, 31]) to magnetization hysteresis loops in the range of  $\pm 50 \text{ kOe}$ .

## 3. Results and discussion

Studies were performed exploring the influence of film thickness and the following three thermal processing parameters: peak annealing  $T$ , the  $T$  ramp and cooling rates, and the annealing dwell time.

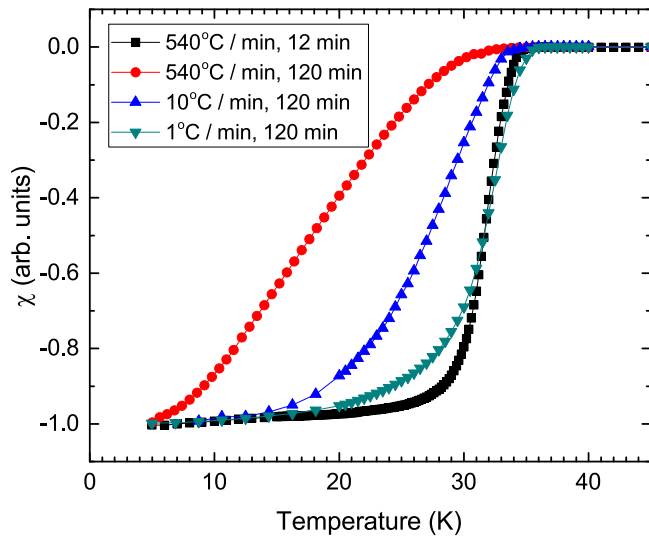


**Figure 1.** Temperature dependence of the magnetic susceptibility,  $\chi(T)$ , for 650 nm thick  $\text{MgB}_2$  films made by Mg vapor annealing at 850 °C with different ramp rates and annealing dwell times, demonstrating that longer dwell times depress  $T_c$  and broaden the superconducting transition.

### 3.1. Peak annealing temperature dependence

Since a wide range of Mg vapor annealing  $T_s$  of 700–950 °C has been reported [1, 5, 18, 23, 24, 32–34, 25], our first set of experiments involved the optimization of reaction  $T$ . A series of samples with 450 nm thick B films were annealed for 120 min at 650 °C, 750 °C, 850 °C, and 950 °C with a ramp rate of 10 °C min<sup>-1</sup>. Films annealed at 650 °C did not superconduct. Films annealed at 750 °C had a depressed  $T_c$  of 30 K and a broad transition, indicating film inhomogeneity. Annealing at 950 °C resulted in films with a  $T_c$  of 28 K, with such a broad transition that the superconducting state was not fully reached even at 5 K. The best superconducting properties were obtained by annealing at 850 °C, yielding a  $T_c$  of 31 K and a sharp transition. Hence, an annealing  $T$  of 850 °C was selected in our subsequent heat treatment experiments.

### 3.2. Annealing dwell time and ramp rate dependencies

Figure 1 shows  $\chi(T)$  curves for 650 nm thick  $\text{MgB}_2$  films made by Mg vapor annealing at 850 °C with several ramp rates and annealing dwell times. All four films from figure 1 exhibit a superconducting transition and reach a fully superconducting state at the lowest measurement  $T$  of 5 K. For 120 min anneals, an increase in the ramp rate results in a monotonic decrease in  $T_c$  and a corresponding increase in the width of the superconducting transition. However, for the fastest ramp rate of 540 °C min<sup>-1</sup>, a short 12 min anneal produces the highest  $T_c$  and the sharpest transition, indicative of high film quality.

The reduction in  $T_c$  for a longer dwell time of 120 min can be correlated with film oxidation. Figure 2 shows representative RBS spectra from  $\text{MgB}_2$  films made by Mg vapor annealing at 850 °C with a ramp rate of 540 °C for 12 and 120 min. This figure first illustrates the use of RBS for simultaneous measurements of the film composition and

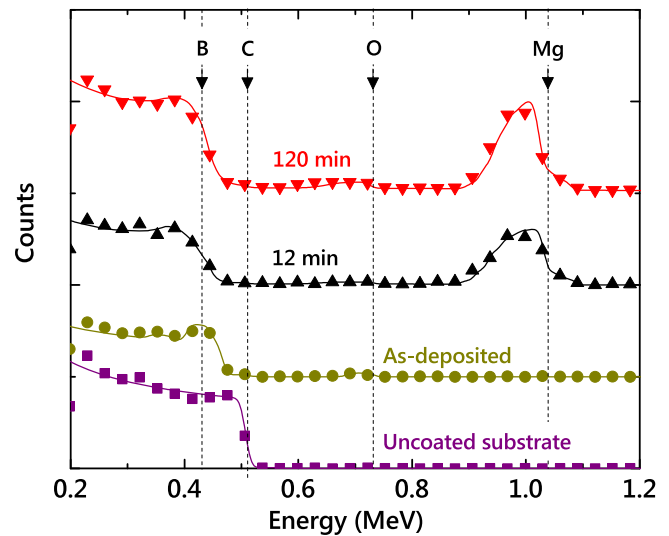


**Figure 2.** RBS spectra from 160 nm thick  $\text{MgB}_2$  films made by Mg vapor annealing at 850 °C with a ramp rate of 540 °C min<sup>-1</sup> for 12 and 120 min, as indicated. Spectra from an as-deposited (un-annealed) film and an uncoated carbon substrate are also shown for comparison. Spectra are vertically offset for clarity. Elemental surface edges are marked by arrows. Symbols are data, while lines are results of RUMP code simulations. Only every tenth experimental point is shown.

thickness even for the case of pure B films. Indeed, although the scattering from B is manifested at lower energies than scattering from heavier C atoms of the glassy carbon substrate, the thickness of the B containing layer is proportional to the shift of the C signal from the substrate, while the formation of  $\text{MgB}_2$  and surface oxidation are indicated by clearly separated Mg and O peaks. Simulations of RBS spectra (figure 2) and companion ERDA spectra (not shown) reveal that as-deposited B films have ~5 and ~10 at% of O and H, respectively. This matches the purity of the deposition target used, also measured by RBS. After Mg vapor annealing,  $\text{MgB}_2$  films have H content of ~5–10 at%. The two films from figure 2 annealed for 12 and 120 min have a composition of  $\text{Mg}_{1.2}\text{B}_2\text{O}_{0.1}$  and  $\text{Mg}_{1.3}\text{B}_2\text{O}_{0.2}$ , respectively, uniform over the depth of the film. This indicates a larger O uptake for longer anneals. Similar O uptake has also been observed in previous studies, proceeding via the incorporation of O into the  $\text{MgB}_2$  matrix as  $\text{MgB}_{2-x}\text{O}_x$  precipitates and the formation of MgO and  $\text{B}_2\text{O}_3$  decorating the film surface and grain boundaries [35–37]. Moreover, depth-resolved RBS measurements have revealed no evidence of inhomogeneity or the presence of unreacted B even for thicker films.

### 3.3. Film thickness dependence

The influence of film thickness on the superconducting properties is illustrated by figure 3 (left axis), which summarizes  $T_c$  values for different annealing conditions. It is seen that  $T_c$  decreases monotonically with film thickness in all the cases. Although a similar reduction in  $T_c$  for thinner films has been observed in several previous studies [14, 34, 38], the physics behind this phenomenon remains a puzzle. A reduction in  $T_c$  in thinner films could be related to lattice elastic

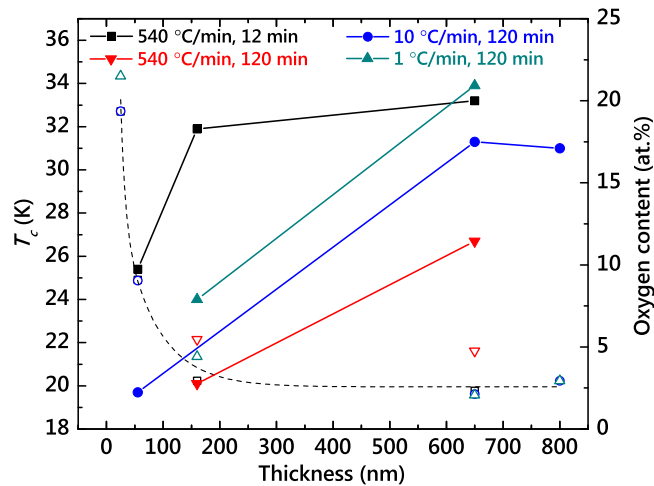


**Figure 3.** Dependence of (left axis, closed symbols)  $T_c$  and (right axis, open symbols) O content on film thickness for  $\text{MgB}_2$  films made by Mg vapor annealing at 850 °C with different ramp rates and annealing dwell times. Solid lines are guides to the eye.

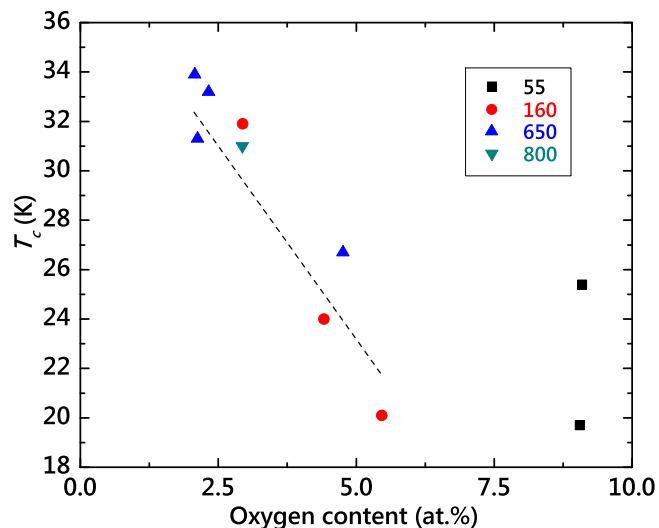


**Figure 4.** Dependence of  $T_c$  on O content (determined by RBS) for  $\text{MgB}_2$  films with different thicknesses indicated in legend (in nanometres). The dashed line is a linear fit to data for 160–800 nm thick films, revealing a slope of  $3.1 \pm 0.2$  K/(at%) and an intercept of 39 K.

strain, disorder (i.e., point and extended defects), or impurities such as O.

The situation is clarified by figure 3 (right axis), which plots RBS-measured O content in the same films, showing that thinner films are more oxidized. Oxygen content rapidly increases with decreasing film thickness below  $\sim 200$  nm. The correlation between O content and  $T_c$  is better illustrated by figure 4, revealing that, for 160–800 nm thick films, all the data points follow a linear dependence with a slope of  $3.1 \pm 0.2$  K/(at%) and an intercept of 39 K. Such a direct correlation between O content and  $T_c$  strongly suggests that O is inimical to the superconducting state of  $\text{MgB}_2$ . An extrapolation of the linear dependence of figure 4 predicts that the superconductivity will be completely suppressed for films with O content above  $\sim 13$  at%. This is in agreement with the

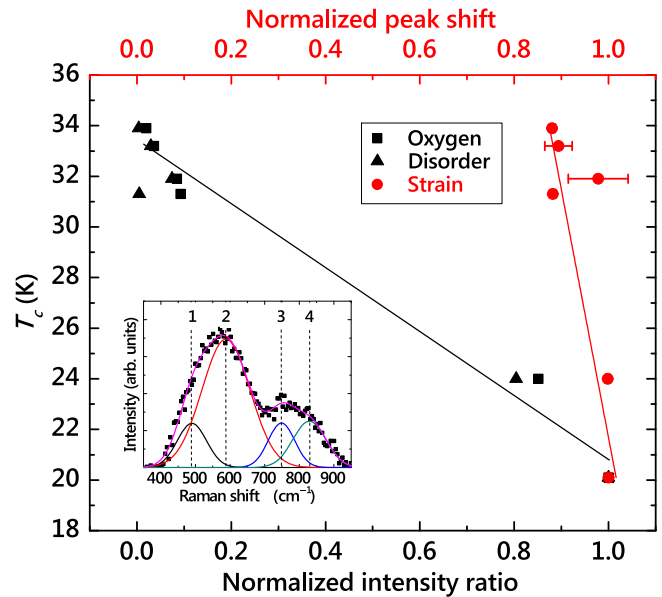


**Figure 5.** Dependence of  $T_c$  on normalized values of the shift of Raman peak 2 (labeled 'Strain') and the intensity ratios of Raman peaks 3 and 2 (labeled 'Disorder') and peaks 4 and 2 (labeled 'Oxygen'). Solid lines are guides to the eye. The inset shows a representative Raman spectrum (after linear background subtraction) of a  $\text{MgB}_2$  film made by Mg vapor annealing for 12 min at 850 °C with a ramp rate of 540 °C min<sup>-1</sup>, defining peaks 1–4 and showing results of peak fitting.

observation that none of the 25 nm thick  $\text{MgB}_2$  films, which have more than 13 at% of O (figure 3 (right axis)), displays a superconducting transition. Interestingly, figure 4 also shows that data points for 55 nm thick films do not fall on the line defined by data for thicker films. This suggests additional complicating factors in such thin films, which are discussed below.

The compositional analysis by RBS (figures 2–4) does not provide any information about the chemical bonding of O and cannot differentiate whether O is in the form of  $\text{MgB}_{2-x}\text{O}_x$  precipitates,  $\text{B}_2\text{O}_3$ , MgO, or some other oxides. The effect of MgO and  $\text{B}_2\text{O}_3$  phases on  $T_c$  can, however, be ruled out since magnetometry-based  $T_c$  measurements reflect the properties of superconducting and magnetic phases and are not directly affected by inclusions or surface layers of non-superconducting and non-magnetic MgO and  $\text{B}_2\text{O}_3$ . Superconducting properties could, however, be affected indirectly by lattice strain associated with O-containing inclusions. Indeed, O incorporation into the  $\text{MgB}_2$  lattice is expected to produce lattice strain, and a correlation between  $T_c$  and lattice strain (monitored as a change in the  $c$ -axis lattice parameter) has been pointed out by Putti *et al* [39].

To better understand effects of lattice disorder, strain, and O content on  $T_c$ ,  $\text{MgB}_2$  films were characterized by Raman spectroscopy. The inset in figure 5 shows a representative Raman spectrum of a  $\text{MgB}_2$  film. This spectrum consists of four well-defined peaks, labeled 1–4. Peak 2, centered at  $\sim 590$  cm<sup>-1</sup>, originates from the  $E_{2g}$  Raman mode of the  $\text{MgB}_2$  crystal [40–42]. It is the only active mode in a Raman spectrum of a defect-free  $\text{MgB}_2$  crystal, according to a group



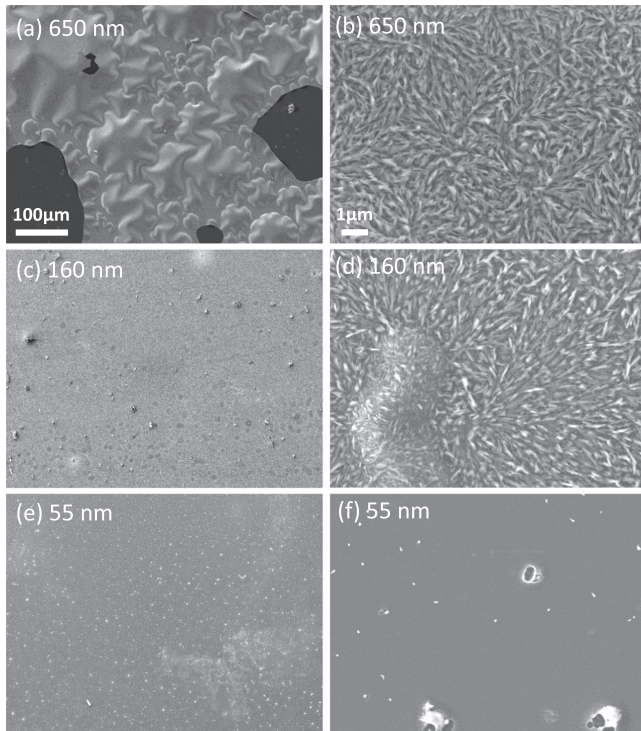


**Figure 6.** SEM images of  $\text{MgB}_2$  films formed by annealing for 12 min at  $850^\circ\text{C}$  with a ramp rate of  $540^\circ\text{C min}^{-1}$ . Film thicknesses are (a), (b) 650 nm, (c), (d) 160 nm, and (e), (f) 55 nm. Images in each column are of the same magnification. Crystallite formation and blistering are suppressed for 55 nm thick films.

theory analysis [40–42]. Peaks 1 and 3, centered at  $\sim 490$  and  $750\text{ cm}^{-1}$ , have been attributed to lattice disorder [40, 41], while peak 4, centered at  $\sim 830\text{ cm}^{-1}$ , can be assigned to O impurities [43]. The large linewidth (full width at half maximum, FWHM) of  $E_{2g}$  indicates a strong electron–phonon coupling [44]. It is expected that the electron–phonon coupling constant (and thus,  $T_c$ ) will be strongly influenced by lattice strain, disorder, and impurities. Lattice strain can be quantified by the frequency shift of the  $E_{2g}$ -related peak 2, while disorder and O content can be quantified as the ratios of intensities of peaks 3 and 4, respectively, to the intensity of the main peak 2.

The relation between  $T_c$  and values strain, disorder, and O content measured by Raman spectroscopy are shown in figure 5, where  $T_c$  decreases linearly with O content. This is in agreement with the trend observed in RBS measurements (figure 4). In fact, the normalized intensity of Raman peak 4 scales linearly with RBS-measured O content and can, thus, be used to quantify O impurities in  $\text{MgB}_2$  [43]. Figure 5 also shows that  $T_c$  decreases with increasing amount of lattice disorder and strain. Future experiments with independent control of O content, elastic strain, and the concentration and type of lattice defects, coupled with theoretical and modeling work, are needed to shed light on the defect physics of superconducting behavior of  $\text{MgB}_2$ .

With the superconducting character of the films established, SEM imaging was performed to assess surface texture and roughness. Figure 6 shows representative low and high magnification SEM images of three  $\text{MgB}_2$  films with

thicknesses of 650 nm (figures 6(a) and (b)), 160 nm (figures 6(c) and (d)), and 55 nm (figures 6(e) and (f)). These films were made by annealing for 12 min at  $850^\circ\text{C}$  with a ramp rate of  $540^\circ\text{C min}^{-1}$ .

It is seen that the 55 nm thick film (figures 6(e) and (f)) displays a smooth surface. The surface is, however, decorated by small ( $\sim 7\text{ nm}$  in diameter) nanoparticles of alloys of Fe, Ni, and Cu, as revealed by SEM-based energy dispersive x-ray spectroscopy measurements. The concentration of these metal impurities in the films, measured by RBS, matches that in the B sputtering target. These impurities precipitate during the  $\text{B} \rightarrow \text{MgB}_2$  conversion process. Aside from these surface precipitates, the 55 nm thick film is smooth and uniform, with no discernible texture. The role of such impurities in film growth is unclear, but it is possible that they affect the film growth as, for example, in the case of surfactant-mediated epitaxy [45, 46]. Figures 6(b) and (d) show that the thicker films are highly textured, with elongated crystallites covering the entire film surface. Based on particle analysis, 160 nm (figure 6(d)) and 650 nm (figure 6(b)) films have average crystallite widths of 11 and 10 nm, respectively. This indicates the presence of multiple nucleation sites and crystal growth proceeding from the B/Mg (solid/vapor) interface, and is in agreement with numerous previous reports of highly textured surfaces of non-epitaxial  $\text{MgB}_2$  films [9, 18, 22, 32]. In thinner films (25 and 55 nm) such multiple crystallite formation is not observed, leading to a smooth surface with a root-mean-square (rms) roughness of 1.1 nm (for areas without alloy nanoparticles), as opposed to a rms roughness of 37.9 nm for 160 nm thick films decorated by elongated crystallites.

The low-magnification SEM of figure 6 reveal that, for the thickest film (figure 6(a)), significant blistering occurs, with some regions showing complete film delamination evidenced as black regions in figure 6(a). The thinner (160 nm thick) film in figure 6(c) does not show such extreme blistering, though occasional smaller blisters are evident in higher magnification imaging such as shown in figure 6(d). In contrast, the thinnest films (25 and 55 nm) do not exhibit blistering (figure 6(e)). Such blistering can be attributed to compressive stresses due to a difference in the coefficient of thermal expansion between glassy carbon ( $3 \times 10^{-6}\text{ K}^{-1}$ ) [47] and B ( $\sim 6 \times 10^{-6}\text{ K}^{-1}$ ) [48], presumably exacerbated by poor adhesion of the film. Furthermore, the nearly twofold increase in volume of the film during vapor processing likely imposes an upper limit on stable film thickness, irrespective of the stress related to thermal expansion. While thicker films are not the focal point of this study, excessive delamination has been observed for films thicker than 900 nm.

Figure 7 shows a Bean-model-derived magnetic field dependence of  $J_c$  for a representative 160 nm thick film at temperatures of 15, 20, and 25 K. The  $\text{MgB}_2$  films exhibit  $J_c \sim 10^6\text{ A cm}^{-2}$ , which is comparable or larger than  $J_c$  of many epitaxial films reported in the literature [2, 5, 6, 31, 49, 50], although  $J_c$  does drop rapidly with increasing field. The maximum value is also lower than record-high  $J_c$  values reported for high-purity HPCVD-grown films [2, 51] although with the benefit of much greater film

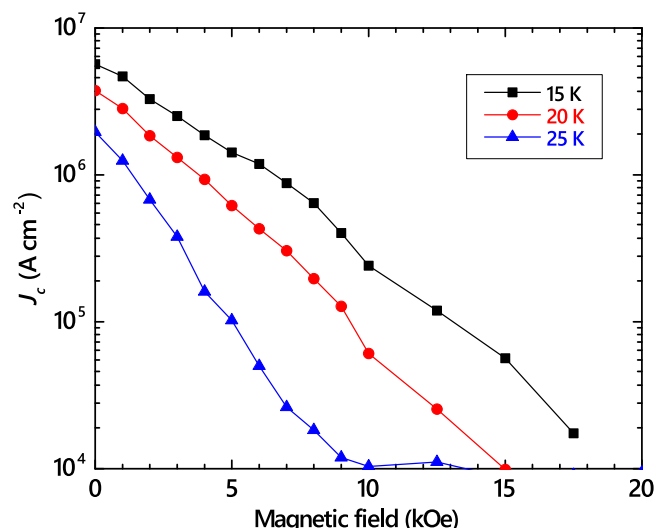


**Figure 7.** Critical current density determined from the Bean critical state model analysis for a 160 nm thick MgB<sub>2</sub> film made by annealing for 12 min at 850 °C with a ramp rate of 540 °C min<sup>-1</sup>.

stability to corrosion in air [52]. Indeed, we have not found any degradation of the superconducting properties of our films after storage in laboratory air for several months.

Finally, the above values of  $T_c$  and  $J_c$  meet the requirements for levitation suggested by the modeling performed, and the smooth surfaces achieved for thin films are amenable to the symmetry requirements imposed by ICF. While further work is required to demonstrate and optimize deposition on spherical fuel capsules, these initial results are promising for the levitation application.

#### 4. Conclusions

We have demonstrated that thin, conformal MgB<sub>2</sub> films on glassy carbon substrates can be made in an inherently non-epitaxial film growth regime by a straightforward fabrication method involving thermal processing of sputter-deposited B precursor films in a Mg vapor atmosphere. The best superconducting properties have been obtained for a short annealing dwell time of 12 min at 850 °C with fast temperature ramp and cool rates of 540 °C min<sup>-1</sup>. Films with thicknesses of 55 nm and below exhibit smooth surfaces, while thicker films display a highly textured surface indicative of multiple nucleation of crystallites. The depression of the superconducting transition temperature has been correlated with lattice disorder and oxygen content. Future systematic studies are needed to explore more complex annealing  $T(t)$  profiles and to minimize the O uptake in ultra-thin films during processing.

#### Acknowledgments

This work was performed under the auspices of the US DOE by LLNL under Contract DE-AC52-07NA27344 and was

supported by the LLNL-LDRD program under Project No. 17-ERD-040.

#### ORCID iDs

A A Baker <https://orcid.org/0000-0003-0700-0858>

L B Bayu Aji <https://orcid.org/0000-0003-1557-3023>

#### References

- [1] Nagamatsu J, Nakagawa N, Muranaka T, Zenitani Y and Akimitsu J 2001 Superconductivity at 39 K in magnesium diboride *Nature* **410** 63
- [2] Xi X X 2009 MgB<sub>2</sub> thin films *Supercond. Sci. Technol.* **22** 043001
- [3] Nath M and Parkinson B A 2007 Superconducting MgB<sub>2</sub> nanohelices grown on various substrates *J. Am. Chem. Soc.* **129** 11302
- [4] Cunnane D, Kawamura J H, Acharya N, Wolak M A, Xi X X and Karasik B S 2016 Low-noise THz MgB<sub>2</sub> Josephson mixer *Appl. Phys. Lett.* **109** 112602
- [5] Kang W N, Kim H-J, Choi E-M, Jung U J and Lee S-I 2001 MgB<sub>2</sub> superconducting thin films with a transition temperature of 39 Kelvin *Science* **292** 1521
- [6] Zeng X *et al* 2002 In situ epitaxial MgB<sub>2</sub> thin films for superconducting electronics *Nat. Mater.* **1** 35
- [7] Rowell J 2002 Magnesium diboride: superior thin films *Nat. Mater.* **1** 5
- [8] Cybart S A *et al* 2014 Large voltage modulation in magnetic field sensors from two-dimensional arrays of Y-Ba-Cu-O nano Josephson junctions *Appl. Phys. Lett.* **104** 062601
- [9] Tan T, Wolak M A, Xi X X, Tajima T and Civalé L 2016 Magnesium diboride coated bulk niobium: a new approach to higher acceleration gradient *Sci. Rep.* **6** 35879
- [10] Moon F C and Chang P-Z 1994 *Superconducting Levitation—Applications to Bearings and Magnetic Transportation* (New York: Wiley-Interscience) (<https://doi.org/10.1002/9783527617524>)
- [11] Yoshida H, Katakami K, Sakagami Y, Azechi H, Nakarai H and Nakai S 1993 Magnetic suspension of a pellet for inertial confinement fusion *Laser Part. Beams* **11** 455
- [12] Aleksandrova I V and Koresheva E R 2017 Review on high repetition rate and mass production of the cryogenic targets for laser IFE *High Power Laser Sci. Eng.* **5** E11
- [13] Clark D S, Kritcher A L, Milovich J L, Salmonson J D, Weber C R, Haan S W, Hammel B A, Hinkel D E, Marinak M M, Patel M V and Sepke S M 2017 Capsule modeling of high foot implosion experiments on the national ignition facility *Plasma Phys. Control. Fusion* **59** 055006
- [14] Zhang C, Wang Y, Wang D, Zhang Y, Liu Z-H, Feng Q-R and Gan Z-Z 2013 Suppression of superconductivity in epitaxial MgB<sub>2</sub> ultrathin films *J. Appl. Phys.* **114** 023903
- [15] Fan Z Y, Hinks D G, Nathan Newman and Rowell J M 2001 Experimental study of MgB<sub>2</sub> decomposition *Appl. Phys. Lett.* **79** 87
- [16] Shen Y, Gandikota R, Singh R K, Hunte F L, Jaroszynski J, Larbalestier D C, Rowell J M and Newman N 2008 A novel technique for synthesizing MgB<sub>2</sub> thin films with high upper critical fields *Supercond. Sci. Technol.* **21** 085009
- [17] Moeckly B H and Ruby W S 2006 Growth of high-quality large-area MgB<sub>2</sub> thin films by reactive evaporation *Supercond. Sci. Technol.* **19** L21
- [18] Zhai H Y, Christen H M, Zhang L, Paranthaman M, Cantoni C, Sales B C, Fleming P H, Christen D K and Lowndes D H

- 2001 Growth mechanism of superconducting  $\text{MgB}_2$  films prepared by various methods *J. Mater. Res.* **16** 2759
- [19] Andrade E, Chromik Š, Jergel M, Jergel M, Falcony C, Štrbík V, Rocha M F and Zavala E P 2003 Study of the superconducting  $\text{MgB}_2$  films by ion beam analysis methods *Thin Solid Films* **433** 103
- [20] Cheang-Wong J C, Jergel M, Jergel M, Chromik Š, Štrbík V and Falcony C 2003 RBS characterization of  $\text{MgB}_2$  superconducting films annealed *ex situ* and *in situ* *Supercond. Sci. Technol.* **16** 879
- [21] Chromik Š, Huran J, Štrbík V, Španková M, Vávra I, Bohne W, Röhrich J, Strub E, Kováč P and Stanček S 2006 Nanogranular  $\text{MgB}_2$  thin films on SiC buffered Si substrates prepared by an *in situ* method *Supercond. Sci. Technol.* **19** 577
- [22] Putri W B K, Kang B, Van Duong P and Kang W N 2015 Reducing delamination in  $\text{MgB}_2$  films deposited on hastelloy tapes by applying SiC buffer layers *Thin Solid Films* **590** 80
- [23] Jones M E and Marsh R E 1954 The preparation and structure of magnesium boride,  $\text{MgB}_2$  *J. Am. Chem. Soc.* **76** 1434
- [24] Hur N, Sharma P A, Guha S, Cieplak M Z, Werder D J, Horibe Y, Chen C H and Cheong S-W 2001  $\text{MgB}_2$  films on boron crystals with onset  $T_C$  of 41.7 K *Appl. Phys. Lett.* **79** 4180
- [25] Bu S-D *et al* 2002 Synthesis and properties of c-axis oriented epitaxial  $\text{MgB}_2$  thin films *Appl. Phys. Lett.* **81** 1851
- [26] Chu W-K, Mayer J W and Nicolet M-A 1978 *Backscattering Spectroscopy* (New York: Academic) (<https://doi.org/10.13140/RG.2.1.1948.0807>)
- [27] Tirira J, Serruys Y and Trocellier P 1996 *Forward Recoil Spectrometry: Applications of Hydrogen Determination in Solids* (Berlin: Springer) (<https://doi.org/10.1007/978-1-4613-0353-4>)
- [28] Doolittle L R 1985 Algorithms for the rapid simulation of Rutherford backscattering spectra *Nucl. Instrum. Methods Phys. Res. B* **9** 344
- [29] Stavrou E, Ahart M, Mahmood M F and Goncharov A F 2013 Probing the different spatial scales of Kel F-800 polymeric glass under pressure *Sci. Rep.* **3** 1290
- [30] Bean C P 1962 Magnetization of hard superconductors *Phys. Rev. Lett.* **8** 250
- [31] Kim H-J, Kang W N, Choi E-M, Kim M-S, Kim K H P and Lee S-I 2001 High current-carrying capability in c-axis-oriented superconducting  $\text{MgB}_2$  thin films *Phys. Rev. Lett.* **87** 087002
- [32] Paranthaman M *et al* 2001 Superconducting  $\text{MgB}_2$  films via precursor postprocessing approach *Appl. Phys. Lett.* **78** 3669
- [33] Cunningham C E, Petrovic C, Lapertot G, Bud'ko S L, Laabs F, Straszheim W, Finnemore D K and Canfield P C 2001 Synthesis and processing of  $\text{MgB}_2$  powders and wires *Physica C* **353** 5
- [34] Dai Q, Wang Y, Ma X, Yang Q, Zhang H, Nie R, Feng Q and Wang F 2012 20 nm  $\text{MgB}_2$  superconducting film with  $T_C$  above 34K and  $J_C \sim 10^6 \text{ A cm}^{-2}$  at 30 K *Physica C* **475** 57
- [35] Klie R F, Idrobo J C, Browning N D, Serquis A, Zhu Y T, Liao X Z and Mueller F M 2002 Observation of coherent oxide precipitates in polycrystalline  $\text{MgB}_2$  *Appl. Phys. Lett.* **80** 3970
- [36] Serquis A, Zhu Y T, Peterson D E, Mueller F M, Schulze R K, Nesterenko V F and Indrakanti S S 2002 Degradation of  $\text{MgB}_2$  under ambient environment *Appl. Phys. Lett.* **80** 4401
- [37] Liao X Z, Serquis A C, Zhu Y T, Huang J Y, Peterson D E, Mueller F M and Xu H F 2002 Controlling flux pinning precipitates during  $\text{MgB}_2$  synthesis *Appl. Phys. Lett.* **80** 4398
- [38] Pogrebnnyakov A V, Redwing J M, Jones J E, Xi X X, Xu S Y, Li Q, Vaithyanathan V and Schlom D G 2003 Thickness dependence of the properties of epitaxial  $\text{MgB}_2$  thin films grown by hybrid physical-chemical vapor deposition *Appl. Phys. Lett.* **82** 4319
- [39] Putti M, Vaglio R and Rowell J M 2008 Radiation effects on  $\text{MgB}_2$ : a review and a comparison with A15 superconductors *Supercond. Sci. Technol.* **21** 043001
- [40] Bohnen K-P, Heid R and Renker B 2001 Phonon dispersion and electron-phonon coupling in  $\text{MgB}_2$  and  $\text{AlB}_2$  *Phys. Rev. Lett.* **86** 5771
- [41] Hlinka J, Gregora I, Pokorný J, Plecenik A, Kúš P, Satrapinsky L and Beňačka Š 2001 Phonons in  $\text{MgB}_2$  by polarized Raman scattering on single crystals *Phys. Rev. B* **64** 140503
- [42] Goncharov A F, Struzhkin V V, Gregoryanz E, Hu J, Hemley R J, Mao H-K, Lapertot G, Bud'ko S L and Canfield P C 2001 Raman spectrum and lattice parameters of  $\text{MgB}_2$  as a function of pressure *Phys. Rev. B* **64** 100509
- [43] Rafailov P M, Bahrs S and Thomsen C 2001 The Raman spectra of  $\text{MgB}_2$  and its potential impurity phases *Phys. Status Solidi b* **226** R9
- [44] Yildirim T *et al* 2001 Giant anharmonicity and nonlinear electron-phonon coupling in  $\text{MgB}_2$ : a combined first-principles calculation and neutron scattering study *Phys. Rev. Lett.* **87** 037001
- [45] Egelhoff W F Jr and Steigerwald D A 1989 The role of adsorbed gases in metal on metal epitaxy *J. Vac. Sci. Technol.* **7** 2167
- [46] Van der Vegt H A, Van Pinxteren H M, Lohmeier M, Vlieg E and Thornton J M C 1992 Surfactant-induced layer-by-layer growth of Ag on Ag (111) *Phys. Rev. Lett.* **68** 3335
- [47] Kuwabara M, Sato M, Onishi Y, Visokay M R, Hayashi H, Inoue H and Muramatsu K 1993 Co alloy media made on amorphous carbon substrate *J. Appl. Phys.* **73** 6686
- [48] Lundström T, Lönnberg B and Bauer J 1998 Thermal expansion of  $\beta$ -rhombohedral boron *J. Alloys Compd.* **267** 54
- [49] Wang Y, Zhuang C, Sun X, Huang X, Fu Q, Liao Z, Yu D and Feng Q 2009 Ultrathin epitaxial  $\text{MgB}_2$  superconducting films with high critical current density and  $T_C$  above 33 K *Supercond. Sci. Technol.* **22** 125015
- [50] Eom C B *et al* 2001 High critical current density and enhanced irreversibility field in superconducting  $\text{MgB}_2$  thin films *Nature* **411** 558
- [51] Xu S Y, Wertz Qi Li, E, Hu Y F, Pogrebnnyakov A V, Zeng X H, Xi X X and Redwing J M 2003 High critical current density and vortex pinning of epitaxial  $\text{MgB}_2$  thin films *Phys. Rev. B* **68** 224501
- [52] Hu H, Feng Q, Wang Y, Zhang Y and Gan Z 2016 Protection of BN for  $\text{MgB}_2$  films against degradation in water *IEEE Trans. Appl. Supercond.* **26** 1